Journal of Engineering Science and Technology Review 18 (2) (2025) 98- 107

Research Article

JOURNAL OF
Engineering Science and Technology Review

www.jestr.org

Optimization of Electromagnetic-Driven Hopkinson Device and Verification by Red Sandstone Test

Jian Gong[1], Aichi Ma[1], Jiaxuan Zhang[1], Shuren Wang[1,2,3,*] , Zhe Li[2] and Dalu Fang[1]

[1]*School of Civil Engineering, Henan Polytechnic University, Jiaozuo 454003, China*
[2]*Jiaozuo Mine Ecological Restoration Field Scientific Observation Research Station of Henan Province, Jiaozuo 454000, China*
[3]*Collaborative Innovation Center of Coal Work Safety, Henan Polytechnic University, Jiaozuo 454003, China*

Received 10 October 2024; Accepted 15 March 2025

Abstract

To address the challenges inherent in traditional pneumatic Split Hopkinson Pressure Bar (SHPB) experimental techniques, including instability at low pressures, inability to attain high pressures, limited reproducibility, and precise stress wave regulation difficulties, a series of experiments were conducted utilizing self-developed electromagnetic drive Hopkinson bars, complemented by numerical simulation methods. Results show that, the matching relationship between coil parameters and projectile muzzle velocity is optimized. Magnetic materials for projectile manufacturing are screened, and eddy current losses in barrels of different materials and bore sizes are analyzed. An aluminum plate is selected as a shield to reduce magnetic leakage and magnetic loss, thereby improving the quality and stability of the shock waveform. Multiple impact experiments were conducted on red sandstone samples to obtain stress-strain curves at different loading strain rates, verifying the stability of the experimental device. The research findings provide the technical support and experimental evidence for the improvement of electromagnetic drive Hopkinson test devices.

Keywords: Hopkinson bar, Electromagnetic-driven, Eddy current loss, Magnetic leakage, Red sandstone

1. Introduction

The Split Hopkinson Pressure Bar (SHPB) experimental technique, as a fundamental method for investigating the dynamic mechanical properties of materials, has seen widespread application in materials science and engineering [1, 2]. This technique is crucial for understanding how materials behave under high-speed, high-energy impacts, which is essential for the development of advanced materials and structures in fields such as aerospace, automotive, and defense.

However, conventional mechanical or gas-driven SHPB techniques face notable limitations in controllability, reaction speed, and repeatability of test data. These limitations can significantly impact the accuracy and reliability of the experimental results, thereby limiting the effectiveness of the technique in high-precision dynamic mechanical testing. For instance, traditional driving forces, such as mechanical springs or compressed gases, are often unstable due to environmental influences such as temperature and pressure variations. This instability can lead to variations in the impact force and speed, which can affect the accuracy of the test results. Additionally, the response time of traditional driving methods is relatively slow, which can limit their application in high-speed testing scenarios.

To address these issues, electromagnetic-driven SHPB experimental technology has emerged as a promising alternative. Electromagnetic drive directly propels the impact bar using electromagnetic force, which eliminates the need for mechanical friction and provides rapid response and high-precision control. These characteristics make electromagnetic-driven SHPB technology particularly suitable for testing material properties under high strain rate conditions, which are critical for understanding the behavior of materials under extreme conditions [3].

Despite its advantages, ensuring the stability of electromagnetic-driven SHPB experimental technology under high strain rate conditions remains a significant challenge. High strain rates can generate significant heat and vibrations, which can affect the performance of the electromagnetic drive system and lead to inaccuracies in the test results. Therefore, ongoing research is focused on developing advanced control systems and materials to improve the stability and reliability of electromagnetic-driven SHPB technology [4, 5].

The SHPB experimental technique is a vital tool for studying the dynamic mechanical properties of materials. However, traditional driving methods have limitations that can affect the accuracy and reliability of the test results. Electromagnetic-driven SHPB technology offers a promising alternative that eliminates mechanical friction, provides rapid response, and allows for high-precision control. However, ensuring stability under high strain rate conditions remains a challenge that requires ongoing research and development.

2. State of the art

As early as 1986, Cowan et al. [6, 7] proposed the concept of electromagnetic launch and discovered its advantages of non-burning and stability. Research on electromagnetic launch technology in China started relatively late [8]. Barr et al. [9] introduced a method for conducting SHPB experiments on soil, using a rigid steel ring to provide plane strain conditions and measuring circumferential strain to infer radial stress. They found that electromagnetic

*E-mail address: w_sr88@163.com
ISSN: 1791-2377
doi:10.25103/jestr.182.12

interference originated from the induced currents in the magnetized pressure bars, while the soil sample had a minimal effect on the interference. Liu et al. [10, 11] developed a mini-SHPB device to enable dynamic mechanical testing of small specimens. Xie et al. [12] developed a dual-projectile electromagnetic-driven SHPB system for studying the dynamic mechanical properties of soft materials. Wang et al. [13] discovered a novel technique that generates bilinear stress waves by superimposing multiple sine waves using Fourier transform. Farbaniec et al. [14] introduced a Torsional Hopkinson Bar system based on Photon Doppler Velocimetry for precise measurement of shear wave propagation under complex conditions, offering superior accuracy and stability compared to traditional strain gauge techniques. Wang et al. [15] demonstrated the effectiveness of the electromagnetic-driven Hopkinson bar for testing the dynamic mechanical behavior of materials in fields such as uniaxial one-way/two-way and dynamic biaxial symmetric compression/tension, interlaminar fracture of composites, and the dynamic Bauschinger effect in metals.

Other scholars, such as Huang et al. [16] developed a mini-Hopkinson bar electromagnetic launcher and achieved controlled speed by accurately controlling capacitor bank discharge with a microcontroller. Cai et al. [17] improved the electromagnetic launch and power supply system for the mini-SHPB, proposing a series-parallel coil array launch structure and energy storage structure to enhance launch speed and equipment efficiency. Nie et al [18] introduced a novel electromagnetic SHPB technique that directly generates controllable stress pulses through electromagnetic conversion, suitable for compression and tension testing of various materials. Khan and Iqbal [19] introduced the design and calibration methods of a SHPB system for dynamic material characterization of concrete, validating its accuracy under high strain rate conditions. Zhao et al. [20] developed a novel impact fatigue test device based on the SHPB system, studying the principles of cyclic loading-resetting and constant amplitude loading. Quillery et al. [21] designed a biaxial compression Hopkinson device with four symmetrical input bars to address multi-axis dynamic loading. Kamble and Tandaiya [22] developed and validated a model using the SHPB system to predict the dynamic compression behavior of bulk metallic glasses at different temperatures. Sobczyk et al. [23] conducted dynamic interaction experiments on soils using the SHPB technique to analyze the response characteristics of cohesive and non-cohesive soils under various conditions, highlighting their importance in the design of protective structures for critical infrastructure.

Despite the progress achieved, the stability of electromagnetic-driven SHPB experimental techniques and the factors influencing it have not been comprehensively studied. These issues may introduce instability in experimental results, thereby compromising the accuracy and repeatability of testing outcomes. This study aims to address these unresolved issues by conducting a series of experiments utilizing electromagnetic-driven SHPB techniques in conjunction with numerical simulation methods. It systematically examines the impact of coil parameters, interactions between the projectile and magnetic field, eddy current losses within the barrel, electromagnetic interference, and the compatibility between the projectile and barrel on the stability of electromagnetic-driven SHPB techniques. By optimizing coil parameters, mitigating electromagnetic interference, and minimizing eddy current losses, this study endeavors to enhance the stability and testing accuracy of the electromagnetic-driven SHPB, ultimately providing technical support for dynamic mechanical property testing of materials.

The rest of this study is organized as follows: Section 3 presents the experimental equipment and experimental procedure. Section 4 describes the experimental results and discussion, and finally, the conclusions are summarized in Section 5.

3. Methodology

3.1 Experimental equipment

An electromagnetic-driven SHPB experimental apparatus was independently developed, leveraging a magnetic reluctance launch device and Hopkinson bar technology. The schematic and physical diagrams of this apparatus are presented in Fig. 1.

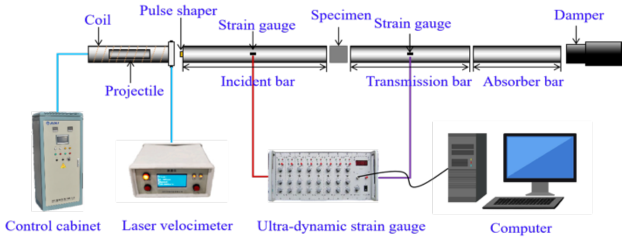

(a) Schematic diagram

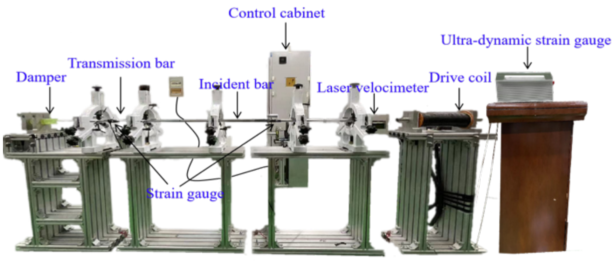

(b) Photograph of experimental apparatus

Fig. 1. Electromagnetic-driven Hopkinson bar experimental apparatus

The projectile, incident bar, and transmission bar each possess a diameter of 20 mm, with respective lengths of 200 mm, 1200 mm, and 800 mm. All these components are constructed from 45-grade steel. The barrel measures 500 mm in length, featuring an inner diameter of 26 mm and an outer diameter of 30 mm. A coil, with an axial length of 300 mm, is wound around the barrel.

3.2 Experimental procedure

When improving the electromagnetic-driven SHPB apparatus, various parameters were configured, including the coil winding method, wire diameter, number of turns, and winding density. Suitable magnetic materials were selected for the projectile, and the surface of the barrel, made of appropriate materials, was grooved. Small rolling balls were attached to the projectile to enhance waveform stability, and the optimized waveform was validated through comparison with numerical simulation results obtained using Abaqus software.

Subsequently, a shield was installed on the coil, and grounding treatment was implemented. After assembling the apparatus, the red sandstone specimens were placed between the bars, and compression impact experiments were conducted at varying loading strain rates. Stress-strain data were recorded using a dynamic strain gauge. Finally, a thorough analysis of the waveform was conducted to verify the stability of the apparatus.

4. Results Analysis and Discussion

4.1 Coil parameters influence on the performance of experimental system

4.1.1 Winding mode effect on experimental system

This study investigates the variation in projectile exit velocity in relation to changes in coil winding method, diameter, number of turns, and winding density using a controlled variable approach. A double-wire parallel winding method was adopted to optimize the electromagnetic coil winding design, as depicted in Fig. 2.

As seen from Fig. 2, the copper wires with the same numbering belong to the same wire set, while those with different numbers are connected in parallel. The input and output wires ultimately converge into a single wire, powered by the same capacitor bank and voltage, facilitating projectile acceleration as the coil discharges.

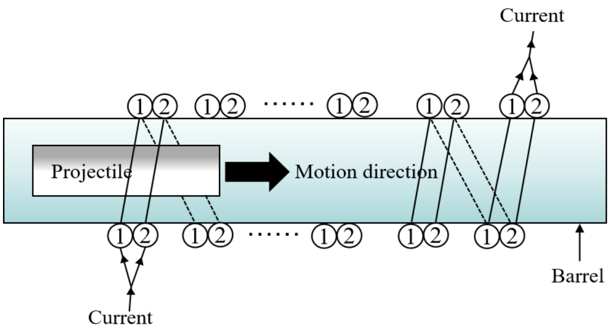

Fig. 2. Schematic diagram of double-wire parallel wound coil drive

In this experiment, a compact electromagnetic-driven device was employed, as illustrated in Fig. 3. The coil, serving as a pivotal component of the electromagnetic drive device, was designed with diverse winding methods and layers, resulting in drive coils exhibiting distinct inductance characteristics. These inductance characteristics have a direct impact on the response speed and driving capacity of the electromagnetic drive device. The specific parameters of the compact electromagnetic-driven device are outlined in Table 1.

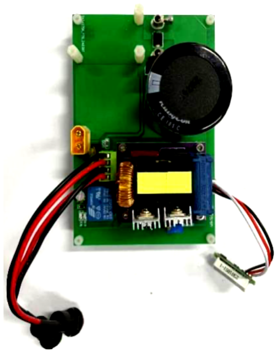

Fig. 3. Small electromagnetic-driven device

During the design and optimization of the electromagnetic-driven experimental apparatus, numerical simulations were conducted using the Ansys Maxwell electromagnetic simulation software under a 150V voltage condition. The simulation results were compared with experimental data, as shown in Table 2.

Table 1. Parameters of the small electromagnetic-driven device

Component name	Attribute	Quantity
DC power supply	12 V	1
Capacitor	450 V, 1000 μf	1
DC-DC high-voltage boost module	90-600 V	1
diode	1000 V, 6 A	1
Enamel-coated wire	Wire diameter 0.8 mm	4
Projectile	Diameter 6 mm, Length 30 mm, Weight 6.6 g	1
Coil resistance	0.6 Ω	1
Coil framework	20 × 8 × 20 mm	1

Table 2. Effects of different coil winding methods and layers on velocity

Winding method	Single-wire winding		Double-wire parallel winding	
Number of layers	3	6	3	6
Simulated velocity (m/s)	4.73	8.63	3.01	7.20
Measured velocity (m/s)	4.62	8.54	2.92	6.54
Relative error (%)	2.40	1.10	3.10	10.10

Based on the results in Table 2, increasing the number of coil winding layers significantly improves projectile launch velocity, regardless of whether a single-wire or double-wire parallel winding is used. The increase in winding layers effectively enhances magnetic field strength, increases inductance, extends the projectile's acceleration path, and optimizes the uniformity of the magnetic field distribution. These factors collectively contribute to a marked increase in projectile launch velocity.

With the same number of winding layers, the projectile velocity for the single-wire winding is higher than that of the double-wire parallel winding, due to differences in inductance and current distribution. In single-wire winding, current is concentrated in a single conductor, generating a stronger magnetic field, which produces greater electromagnetic force, resulting in higher acceleration for the projectile. In the double-wire parallel winding, current is distributed across two conductors. While this effectively reduces resistance and heat generation, the relatively low inductance value leads to reduced magnetic field strength and electromagnetic force. Additionally, the parallel structure in double-wire winding may cause partial magnetic field cancellation, resulting in lower projectile velocity compared to single-wire winding. In summary, single-wire winding was selected for this study.

Although the launch model developed in Maxwell software considers the effect of air resistance on projectile velocity, the predicted velocity is based on the maximum value within the barrel and coil region. In practice, however, the speed sensor can only measure the projectile' s velocity after it exits the barrel, so the actual measured initial velocity is usually lower than the model' s predicted value. Overall, an error within 10% is acceptable in practical testing, which also verifies the stability of the simulation model and the reliability of the conclusions.

4.1.2 Influence of coil diameter on performance of experimental system

Under single-wire winding conditions, we selected three commonly available enamel-coated wires with diameters of 1.5 mm, 1.8 mm, and 2 mm for the coil wire diameter. The initial winding number was set to 1500 turns. Table 3 shows the theoretical lengths and resistances of enamel-coated wires of different diameters required to form a 1500-turn coil. As projectile speed increases with voltage, a voltage of 600 V was chosen in this experiment to ensure safety and extend capacitor bank life. The simulation results are shown in Fig. 4.

Table 3. Parameters of launch coils wound with enamel-coated wires of different diameters

Diameter (mm)	Wire length (m)	Coil resistance (Ω)
1.50	201.588	1.93
1.80	226.532	1.50
2.00	244.920	1.31

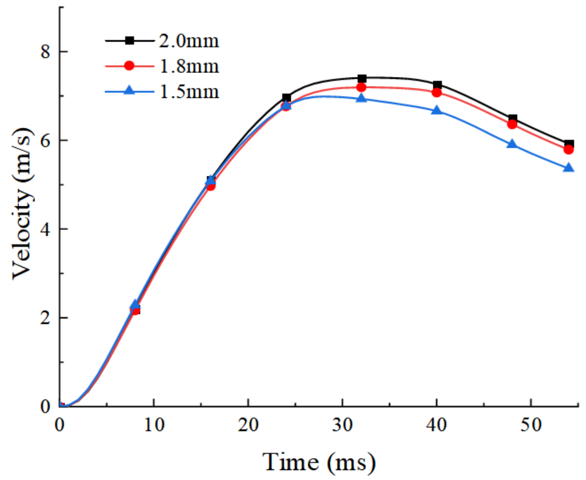

Fig. 4. Relationship between enamel-coated wire diameter and projectile velocity

As shown in Fig. 4, when the diameter of the enamel-coated wire is 2.0 mm, the projectile achieves the highest velocity, followed by 1.8 mm, with the 1.5 mm wire yielding the slowest projectile velocity. This is because thicker enamel-coated wire has a larger conductive cross-sectional area, allowing it to carry higher currents, effectively reducing resistance losses and minimizing heat generation during current flow. Additionally, enamel-coated wire of this diameter has greater mechanical strength and durability, enabling it to withstand mechanical shocks and vibrations during the electromagnetic drive process. In actual coil gun launches, the drive coil must not only handle the radial electromagnetic expansion force but also endure the axial reaction force generated during the launch. Dielectric breakdown and mechanical structural damage are common issues. To improve winding quality, adhesive is used during the coil winding process to secure the coil, effectively preventing movement and deformation while ensuring a uniform distribution of magnetic flux density. Considering the high power requirements, heat dissipation needs, and mechanical stability of the electromagnetic drive, a 2.0 mm enamel-coated wire was selected in this study.

4.1.3 Effect of coil turns on performance of experimental system

Based on the electromagnetic simulation results, a single-wire winding was chosen with an enamel-coated wire diameter of 2.0 mm, a voltage of 600 V, and other parameters held constant. The peak projectile velocity and peak electromagnetic force under different coil turns were compared, with simulation results shown in Fig. 5.

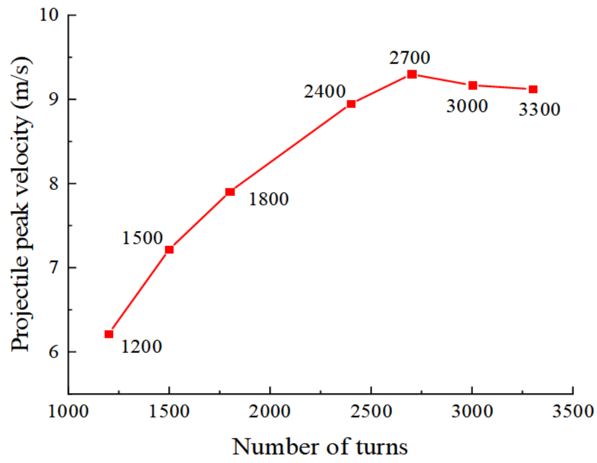

(a) Cuves of projectile peak velocity and number of turns

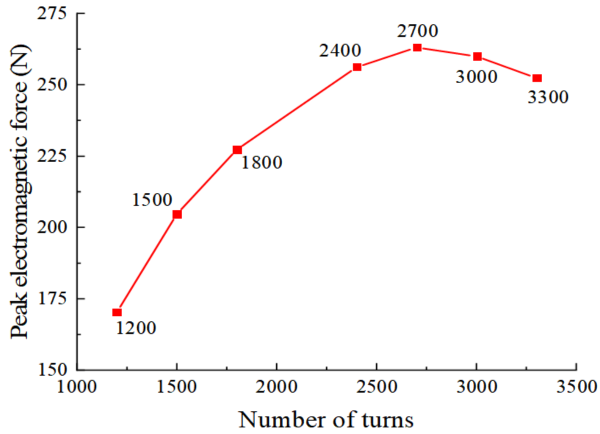

(b) Cuves of electromagnetic force peak and number of turns

Fig. 5. Cuves of projectile peak velocity and electromagnetic force peak with number of turns

Fig. 5 show the relationship curves of projectile peak velocity and peak electromagnetic force with respect to the number of turns. When the number of turns is between 1200 and 2700, both projectile velocity and electromagnetic force increase, with the greatest increase observed from 1200 to 1500 turns. At 2700 turns, the velocity and electromagnetic force reach their respective peaks of 9.3 m/s and 263 Newton. As the number of turns continues to increase beyond this point, both values exhibit a downward trend. These results indicate that changes in the number of turns significantly impact the coil’s peak electromagnetic force. When the coil has a relatively low number of turns, the projectile velocity and electromagnetic force increase with the number of turns.

However, when the number of turns exceeds a certain threshold (2700 turns), the coil’s outer diameter expands, and each additional turn requires a much longer wire length than the previous one, leading to an overall increase in resistance. This effect is limited with fewer turns, but once the critical number of turns is reached, further increases in turns lead to a reduction in electromagnetic force. Due to the small size of the experimental apparatus, an excessive number of winding layers not only increases the difficulty of winding but may also prevent the coil from being fully accommodated. Considering both spatial constraints and electromagnetic performance, 1500 turns were ultimately selected for this study.

4.1.4 Effect of coil density on performance of experimental system

Based on the study of coil winding density, a single-wire winding, 2 mm enamel-coated wire, 1500 turns, and 600 V voltage were selected, with all other conditions remaining constant. In the "front sparse, rear dense" winding method, the first half of the coil is wound with 5 layers, and the second half with 15 layers. The "front dense, rear sparse" winding is the opposite. Fig. 6 shows the effect of coil winding density on projectile velocity.

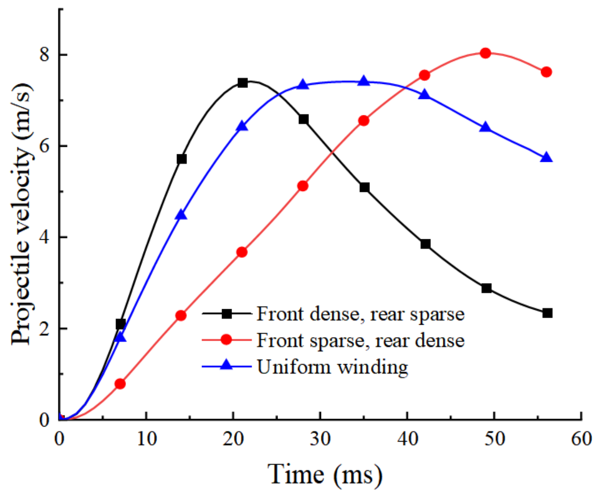

Fig. 6. Effect of coil winding density on projectile velocity

As shown in Fig. 6, the projectile velocity reaches a maximum of 8 m/s with the "front sparse, rear dense" winding method. For uniform winding and "front dense, rear sparse" winding, the velocity is approximately 7 m/s. The "front sparse, rear dense" winding configuration optimizes the magnetic field gradient distribution, allowing the projectile to transition from a weaker magnetic field region to a stronger one during acceleration. This configuration can continuously provide greater acceleration, reduce the resistance from reverse electromagnetic force, and enable the projectile to achieve higher speeds. However, the "front sparse, rear dense" winding method is more complex than uniform winding, as it requires precise control of the coil's turn distribution. Uneven turn distribution may lead to uneven energy distribution, which can result in local overheating and potential damage. Additionally, an uneven magnetic field gradient may cause instability in the projectile's motion. Fig. 7 shows a comparison of electromagnetic force variation over time.

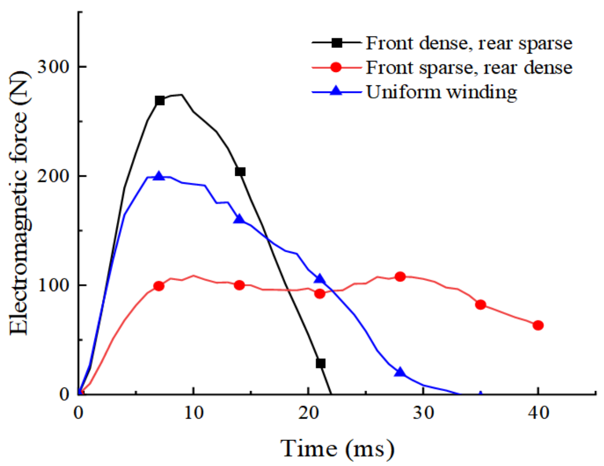

Fig. 7. Comparison of electromagnetic force variation over time

As shown in Fig. 7, the electromagnetic force in the "front dense, rear sparse" coil is initially high but quickly decreases to a negative value over time. Negative electromagnetic force indicates that the projectile is moving in the opposite direction. The uniformly wound coil reaches a higher peak electromagnetic force faster than the "front sparse, rear dense" coil, exhibiting a quicker dynamic response. The electromagnetic force in the uniformly wound coil gradually declines after reaching its peak, with minimal fluctuations. This characteristic makes it suitable for applications requiring rapid electromagnetic force enhancement and relative stability in confined spaces.

Due to the non-uniform turns and spacing in the "front sparse, rear dense" design, magnetic field strength varies significantly across regions. The front section has a weaker magnetic field, while the rear section is stronger. This unevenness can result in inconsistent thrust on the projectile during acceleration, impacting the smoothness of acceleration and projectile stability. Especially during high-speed motion, the trajectory may deviate, or force fluctuations may occur. Under these conditions, the uniformly wound coil demonstrates optimal performance.

In summary, the optimal values of the coil parameters selected for this study are shown in Table 4.

Table 4. Optimal values of coil parameters

Coil winding method	Coil wire diameter (mm)	Number of coil turns	Coil winding density
Single-wire winding	2.0	1500	Uniform winding

4.2 Interaction between magnetic conductive material and external magnetic field

The interaction between the magnetic field and magnetic domains is the core mechanism by which the magnetic field drives the movement of magnetic materials. Within magnetic materials, electron spin and orbital motion generate a magnetic field, forming magnetic domains. Under the influence of an external magnetic field, these magnetic domains realign, causing the overall magnetization of the magnetic material to align with the external field, thereby generating attractive or repulsive forces. By studying the interaction between various magnetic materials and the external magnetic field, the optimal magnetic material was selected for projectile manufacturing to enhance acceleration performance and stability, as shown in Fig. 8.

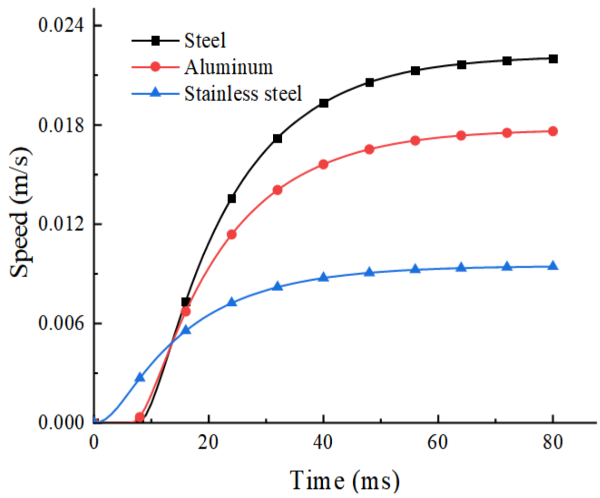

(a) Muzzle velocity for projectiles made from different materials

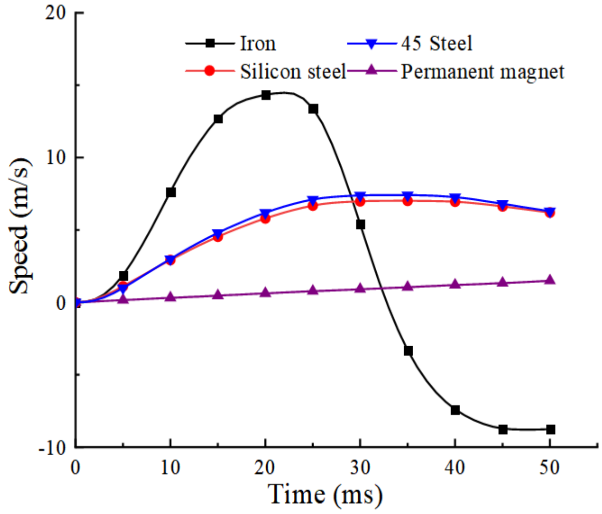

(b) Muzzle velocity for projectiles made from different magnetic materials

Fig. 8. Comparison of muzzle velocity for projectiles made from different materials

Fig. 8(a) shows several common metallic materials, whose velocities are significantly low, around 0.02 m/s. This is due to their low magnetic permeability, and in some cases, they are almost unaffected by the external magnetic field. Consequently, they cannot effectively couple with the electromagnetic field, resulting in insufficient driving force. If the material has good magnetic permeability (such as ferromagnetic materials), the external magnetic field can induce a stronger magnetic field within the material, thereby generating a greater thrust.

As shown in Fig. 8(b), the velocity of an iron projectile can reach a peak of 15 m/s, but over time, the projectile exhibits reverse motion. This is due to the hysteresis effect of iron material. After the electromagnetic field is turned off, the magnetic domains within the iron projectile cannot immediately return to a disordered state, retaining a certain level of residual magnetism. This residual magnetism interacts with the residual magnetic field in the coil. Both 45 steel and silicon steel belong to the category of steel, with similar magnetic permeability, resulting in comparable velocities of around 7.5 m/s. Additionally, iron and silicon steel may fracture during high-speed impact due to their relative brittleness. Permanent magnets exhibit the lowest velocity because their fixed magnetism interferes with the external electromagnetic field, leading to unstable acceleration. In summary, 45 steel, with its higher strength and toughness, is the more suitable choice.

4.3 Analysis of the eddy current effect mechanism in metal barrels

In electromagnetic launch technology, the material and structure of the barrel are critical to system performance. While non-metallic barrels avoid the generation of eddy currents, they have drawbacks such as poor straightness, insufficient inner wall smoothness, and low strength, resulting in an inability to precisely control projectile velocity and very limited service life. High-precision metal barrels, with good straightness, high inner wall smoothness, and high yield strength, are suitable for electromagnetic drive launch devices. However, when the electromagnetic drive device discharges instantaneously, the metal barrel wound with coils generates induced currents, leading to barrel heating, magnetic force loss, and potentially even explosion issues.

A three-dimensional model of the induction coil gun was constructed in the eddy current field solver of ANSYS Maxwell, as shown in Fig. 9.

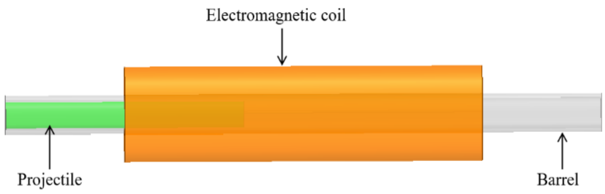

Fig. 9. Three-dimensional simulation model of induction coil gun

4.3.1 Analysis of the impact of metal barrels on eddy current loss

To gain a deeper understanding of the impact of metal barrels on eddy current loss, a comparative numerical simulation was conducted for different metallic materials, as shown in Fig. 10.

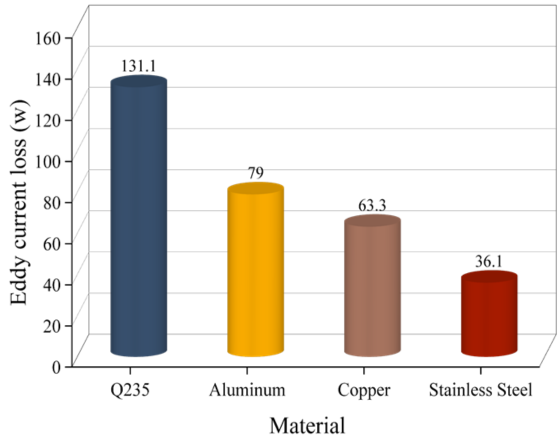

Fig. 10. Eddy current loss in barrels made of different metal materials

As shown in Fig. 10, Q235 steel exhibits the highest eddy current loss at 131.1 W, followed by aluminum and copper. Stainless steel has the lowest eddy current loss, at only 36.1 W. This phenomenon can be attributed to stainless steel's non-magnetic nature and high resistivity. As a non-magnetic material, stainless steel is less permeable to magnetic field lines, which reduces eddy current generation. Additionally, stainless steel's high resistivity further weakens the eddy current effect within it; eddy current strength is inversely proportional to the material's resistivity-the higher the resistivity, the lower the eddy current loss. Based on these characteristics, stainless steel was selected as the barrel material.

4.3.2 Impact analysis of slotting on eddy current loss

As shown in Fig. 11, a 3 mm wide and 400 mm long slot was cut along the length of the stainless steel barrel's surface to break the eddy current loop. This design is essential for reducing eddy current loss in the barrel, as eddy current loss results from energy dissipation caused by induced currents within the barrel material in an alternating magnetic field. This loss not only reduces system efficiency but may also lead to barrel overheating. In this way, when the drive coil discharges, the lack of a closed current loop prevents the formation of induced currents, thereby reducing the heat generated in the barrel. Fig. 12 shows a comparison of current density distribution between the solid barrel and the slotted barrel.

Fig. 11. Processed barrel

As shown in Fig. 12, when the projectile moves to the middle of the barrel, Fig. 12(a) shows that the current density distribution across the barrel is relatively uniform and concentrated. When the ferromagnetic projectile is in a changing magnetic field, an induced electromotive force (EMF) is generated within the conductor, according to Faraday's law of electromagnetic induction. If the conductor is closed, this EMF induces an eddy current within it. Consequently, the current density in this region becomes relatively high. In Fig. 12(b), the current density at both ends of the projectile in the barrel is slightly higher, gradually decreasing outward from this region. The current distribution shows unevenness and a broader range. Compared to 12(a), the overall current density distribution in other areas of the barrel in 12(b) is reduced. By slotting the barrel, eddy current loss was reduced from 36.12 W to 4.88 W, consistent with expectations. To further optimize performance, epoxy resin was added to the slot, smoothing the inner and outer surfaces and reducing friction between the projectile and the barrel.

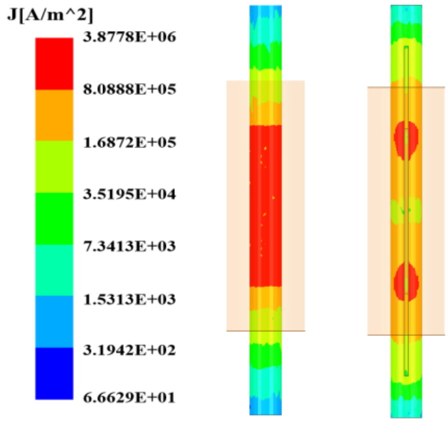

(a) Solid barrel (b) Slotted barrel

Fig. 12. Comparison of current density distribution between solid and slotted barrels

4.3.3 Impact analysis of slot size on eddy current loss

To optimize the barrel slotting design, this study conducted an in-depth analysis of the effects of different slot sizes on eddy current loss and structural strength. The slot depth was fixed at 3 mm, as shown in Table 5.

Table 5 shows the effect of different slot sizes on eddy current loss. The study results indicate a significant decrease in eddy current loss as the slot length and width increase, suggesting that increasing the slot area effectively inhibits the formation and development of eddy currents. Specifically, with a slot length of 400 mm and width of 3 mm, the eddy current loss is reduced to 4.88 W, achieving optimal suppression. However, it is important to note that the slot area cannot be enlarged indefinitely, as an excessively large slot area may compromise the structural strength of the barrel. Balancing eddy current loss and structural strength, this study ultimately selected a slot design with a length of 400 mm, width of 3 mm, and depth of 3 mm.

Table 5. Eddy current loss for different slot sizes

Length (mm)	**200**			**300**			**400**		
Width (mm)	1	2	3	1	2	3	1	2	3
Eddy current loss (w)	30.0	29.10	28.92	13.65	13.44	13.16	5.14	5.01	4.88

4.4 Electromagnetic signal interference suppression and noise reduction techniques

A shielding body was created using a high-conductivity material (aluminum plate). As shown in Fig. 13, this shield effectively reflects and absorbs high-frequency electromagnetic waves while being lightweight, corrosion-resistant, and easy to process. By enclosing the interference source, blocking the electromagnetic signal propagation path, and grounding the equipment through wires, interference suppression and noise reduction are achieved.

Fig. 13. Aluminum plate shield

A gauss meter was used to measure magnetic leakage. In the electromagnetic-driven Hopkinson bar system, the magnetic field is influenced by power supply stability, transient current, material properties, and external environment, and thus is not completely stable. The current in the experiment can reach a high value within a few milliseconds, which may cause significant magnetic field fluctuations. In this experiment, six sets of data were collected at the same position outside the aluminum plate under the same voltage condition (600 V) for comparison, as shown in Fig. 14.

Fig. 14 clearly demonstrates the effectiveness of the aluminum plate as a shield in magnetic field suppression. Under the same voltage conditions, the magnetic induction intensity significantly decreases after the shield is installed. Due to its excellent conductivity, the aluminum plate effectively absorbs and scatters the magnetic field. This phenomenon clearly indicates the effectiveness of the aluminum plate in reducing magnetic leakage. After installing the shield and grounding, the magnetic induction intensity decreased to a minimum of 6 Gs. The enhanced shielding effect not only reduces the risk of electromagnetic interference but also improves the electromagnetic compatibility (EMC) of the device, thereby increasing its stability and reliability in complex electromagnetic environments.

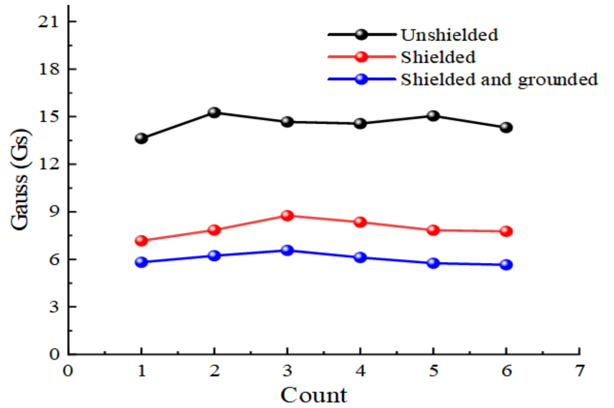

Fig. 14. Comparison of magnetic field intensity under shielded and unshielded conditions

4.5 Effect analysis of projectile-barrel fit on waveform stability

As shown in Fig. 15, the projectile is made of specially treated 45-grade tempered steel, with a length of 200 mm and a diameter of 20 mm. three ball bearings are evenly mounted on the surface of the projectile at each 50 mm interval, with each set of bearings arranged at 120° intervals, totaling 9 bearings.

Fig. 15. Processed projectile

By adding horn bearings to the bullet's surface, friction between the bullet and the inner barrel wall is reduced. Additionally, this modification prevents the bullet from misaligning with the incident rod upon exiting the barrel due to gravitational sagging, thus avoiding waveform errors. Fig. 16 shows the original waveform of the bullet before and after processing.

As shown in Fig. 16, the waveform becomes smoother, and the waveform quality is significantly improved after adding ball bearings to the projectile. This improvement is due to the ball bearings effectively reducing friction between the projectile and the barrel and providing more uniform force distribution upon firing, preventing tilting or asymmetric forces during projectile motion. Additionally, the ball bearings provide a cushioning effect, reducing vibrations and noise caused by collisions between the projectile and the barrel wall.

Fig. 17 shows the empty bar waveform simulated in Abaqus. Compared to Fig. 16(b), the resulting waveform is essentially consistent. This aligns with the propagation law of stress waves: when stress waves propagate through two elastic bars made of the same material, the waves pass through the impact interface without reflection and without waveform superposition. This also indicates that the assembly of the bars in the electromagnetic SHPB device and the bonding of the strain gauges were performed well. Additionally, a clear plateau is observed at the top of the waveform, indicating that a constant strain rate loading was achieved during sub-impact.

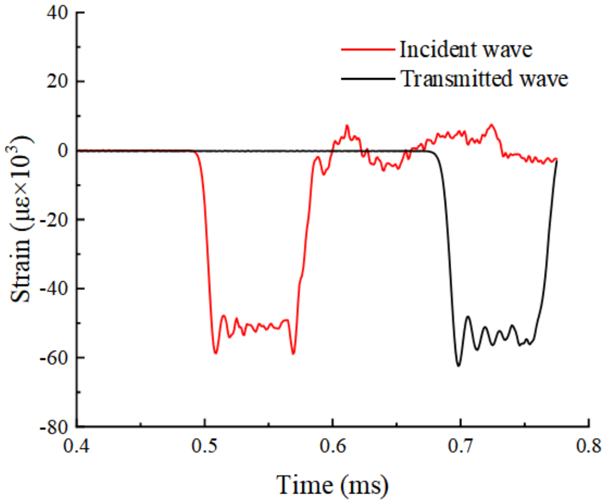

(a) Original waveform without ball bearings

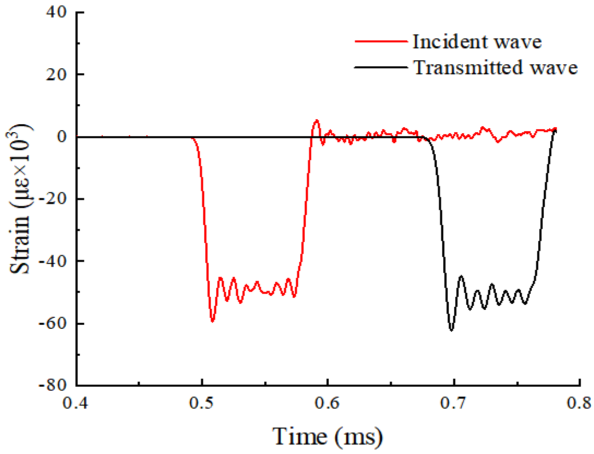

(b) Original waveform with ball bearings

Fig. 16. Original waveform diagram before and after projectile processing

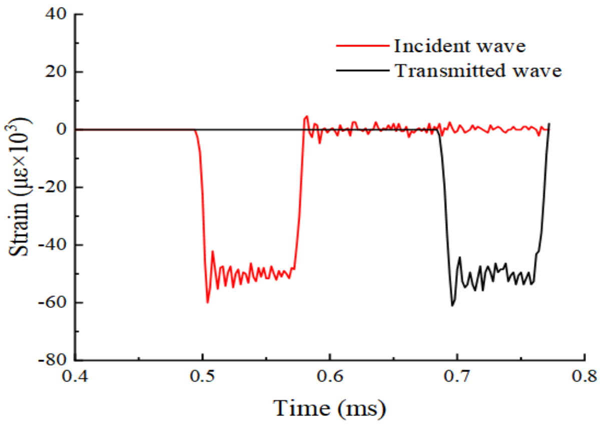

Fig. 17. Empty bar waveform simulated in Abaqus

4.6 Verification analysis of dynamic properties of red sandstone specimens

To further verify the feasibility of the electromagnetic-driven Hopkinson pressure bar experimental technique and apparatus, impact compression validation tests with samples are necessary. Using the dynamic compression test results of red sandstone, the reliability of the device was verified and analyzed. The red sandstone specimen has a diameter of 16 mm and a thickness of 16 mm. According to the one-dimensional stress wave theory, the stress-strain curves of red sandstone under different strain rates are obtained, as shown in Fig. 18.

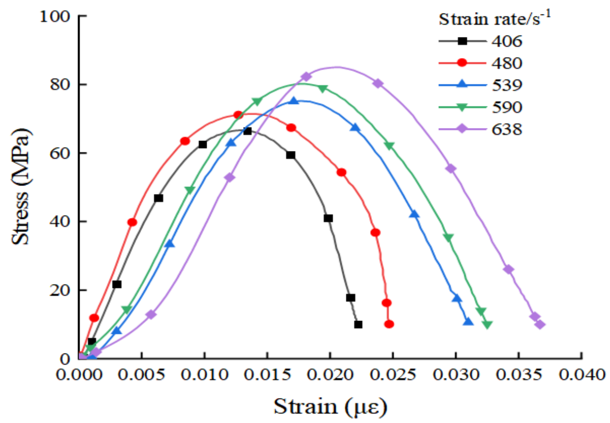

Fig. 18. Stress-strain curves under different loading strain rates

As shown in Fig. 18, the stress-strain curves of the specimen exhibit good dynamic response consistency under different strain rate conditions. With an increase in loading strain rate, both the peak stress and peak strain of the specimen show a gradual upward trend. The results of the compression impact test are consistent with the dynamic mechanical properties of red sandstone [24]. Fig. 19 show five sets of parallel experiments under different voltages.

As shown in Fig 19, the stress-strain curves under the same voltage are generally consistent. Table 6 presents the experimental data under different impact voltages, showing a relatively small standard deviation, indicating low data dispersion and relatively concentrated experimental results. In summary, this demonstrates the high reliability of the electromagnetic-driven SHPB technique and apparatus.

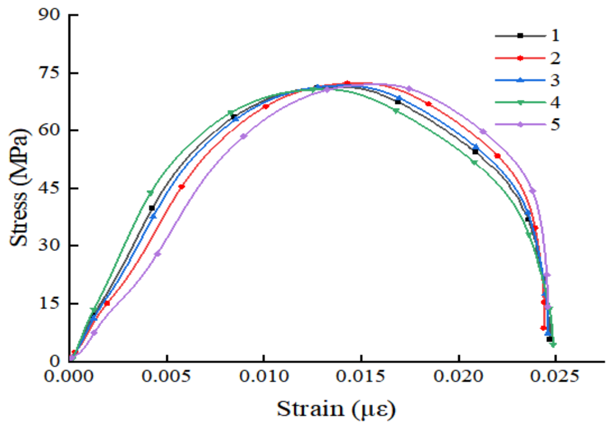

(a) 600 V

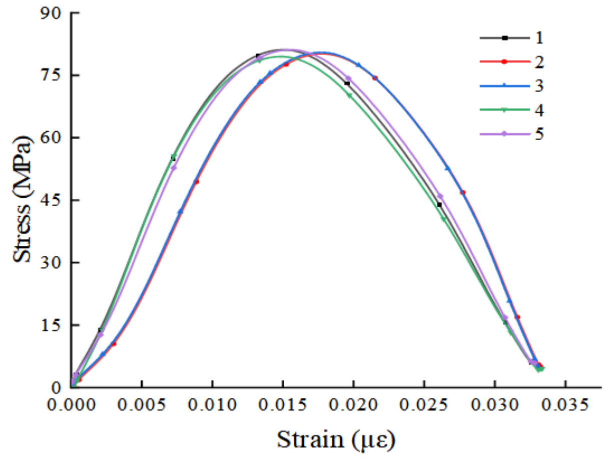

(b) 800 V

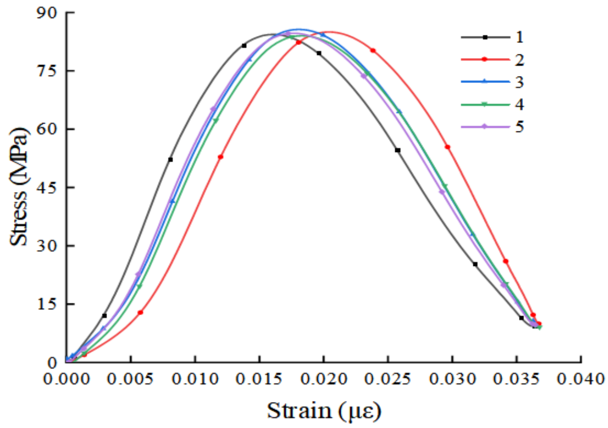

(c) 900 V

Fig. 19. Stress-strain curve at different voltages

Table 6. Experimental data under different impact voltages

Voltage U (V)	Impact velocity (m/s)	Peak stress (MPa)	Standard deviation
600	7.692	72.08 72.4 71.4 71.75 70.77	0.56
800	9.434	80.17 81.15 80.4 79.5 81.1	0.63
900	10.204	85.02 84.36 85.67 84.03 84.69	0.56

5. Conclusions

An independently developed electromagnetic-driven SHPB experimental apparatus was created, optimizing parameters of the electromagnetic coil launch system, barrel eddy current loss, and magnetic leakage. The reliability of this apparatus was validated and analyzed through dynamic compression testing on red sandstone. The main conclusions are obtained as follows:

(1) By selecting a single-wire winding with a 2 mm diameter and 1500 turns, using uniform winding, the projectile launch efficiency was effectively improved, optimizing the performance of the experimental system. 45 steel was selected as the optimal material for projectile manufacturing.

(2) Stainless steel was chosen as the barrel material, and a slotting design was implemented. As the slot area increased, eddy current loss was significantly reduced, effectively suppressing surface eddy current generation, reducing barrel heating, magnetic force loss, and potential explosion risk.

(3) A shield made of low-resistance material (aluminum plate) was grounded to reduce magnetic leakage, decreasing electromagnetic signal interference with strain waves. Adding small ball bearings to the projectile resulted in a smoother original waveform, reduced fluctuations, and significantly enhanced overall stability.

Projectile muzzle velocity is a key indicator for evaluating electromagnetic drive devices. In single-stage electromagnetic drive systems, speed is increased by adjusting circuit parameters such as voltage and capacitance. Higher muzzle velocities can be achieved by accelerating the projectile through multi-stage coils. In electromagnetic-driven SHPB technology, the closed discharge switch and the generation of stress waves are nearly simultaneous. By modifying two identical electromagnetic-driven SHPB systems for dynamic biaxial loading, it becomes possible to study the mechanical properties of materials under multi-axial stress states.

In practical engineering, understanding the triaxial compressive behavior of materials such as concrete and rock is crucial for structural design. Although triaxial testing systems have been developed, the triaxial synchronous loading tests at high strain rates are rare due to experimental limitations. Integrating the electromagnetic-driven device with a triaxial testing system enables single-axis, biaxial, and triaxial synchronous loading on materials like rock and concrete to study their mechanical properties and failure modes under impact loads.

Acknowledgements
This work was financially supported by the National Scholarship Fund of China [2023]-21, Key Project of Natural Science Foundation of Henan Province, China (232300421134), First-Class Discipline Implementation of Safety Science and Engineering (AQ20230103), and Zhongyuan Science and Technology Innovation Leading Talent Program (244200510005), China.

References

[1] T. Fila, *et al.*, “Dynamic impact testing of cellular solids and lattice structures: Application of two-sided direct impact Hopkinson bar,” *Int. J. Impact Eng.,* vol. 148, Feb. 2021, Art. no. 103767.
[2] S. R. Wang, J. Q. Zhao, J. Gong, J. M. Xu, and C. L. Li, “Analysis on energy absorption capacity of MLWC under electromagnetic driving SHPB condition,” *Dyna*, vol. 98, no. 3, pp. 256-264, Jun. 2023.
[3] C. M. A. Silva, P. A. R. Rosa, and P. A. F. Martins, “An innovative electromagnetic compressive split Hopkinson bar,” *Int. J. Mech. Mater. Des.,* vol. 5, no. 3, pp. 281-288, Aug. 2009.
[4] Y. Z. Guo, *et al.*, “Electromagnetic Hopkinson bar: A powerful scientific instrument to study mechanical behavior of materials at high strain rates,” *Rev. Sci. Instrum.*, vol. 91, no. 8, Aug. 2020, Art. no. 081501.
[5] S. R. Wang, X. G. Wu, J. H. Yang, and S. Zhu, “Acoustic emission characteristics and dynamic damage constitutive relation of shale ceramsite concrete subjected to loading tests,” *J. Mater. Civil Eng.*, vol. 32, no. 8, Aug. 2020, Art. no. 04020202.
[6] T. Cowan, *et al.*, “Observation of correlated narrow-peak structures in positron and electron spectra from superheavy collision systems,” *Phys. Rev. Lett.*, vol. 56, no. 5, pp. 444-447, Feb. 1986.
[7] G. H. Shvetsov, P. G. Rutberg, and V. A. Kolikov, “Electric launch in Russia: A review of recent results,” *IEEE Trans. Magn.*, vol. 35, no. 1, pp. 37-43, Jan. 1999.
[8] W. B. Liu, Y. J. Cao, Y. Zhang, J. Wang, and D. W. Yang, “Parameters optimization of synchronous induction coilgun based on ant colony algorithm,” *IEEE Trans. Plasma Sci.*, vol. 39, no. 1, pp. 100-104, Jan. 2011.
[9] A. D. Barr, S. D. Clarke, A. Tyas, and J. A. Warren, “Electromagnetic interference in measurements of radial stress during split Hopkinson pressure bar experiments,” *Exp. Mech.*, vol. 57, no. 5, pp. 813-817, Jun. 2017.
[10] Z. W. Liu, X. M. Chen, X. T. Lv, and H. M. Xie, “A mini desktop impact test system using multistage electromagnetic launch,” *Measurement,* vol. 49, no. 1, pp. 68-76, Mar. 2014.
[11] C. T. Zhang, Z. W. Liu, X. M. Wang, and S. Cai, “Optimization and application of an electromagnetic mini Hopkinson bar device,” *J. Exp. Mech.,* vol. 35, no. 1 , pp. 18-26, Jan. 2020.
[12] B. X. Xie, *et al.*, “A double-projectile electromagnetic-driven SHPB system for soft materials,” *Explos. Shock Waves*, vol. 39, no. 5, pp. 69-75, Oct. 2019.
[13] W. B. Wang, *et al.*, “The achievement of constant strain rates in electromagnetic Hopkinson bar test,” *Int. J. Impact Eng.*, vol. 95, Jan. 2025, Art. no. 105121.
[14] L. Farbaniec, *et al.*, “Assessment of bending waves in torsion Hopkinson bar experiments using photon Doppler velocimetry,” *Int. J. Impact Eng.*, vol. 195, Jan. 2025, Art. no. 105139.
[15] W. B. Wang, *et al.*, “Experimental technique and research progress of electromagnetic Hopkinson bar,” *Adv. Mech.*, vol. 51, no. 4, pp. 729-754, Aug. 2021.
[16] W. K. Huang, G. X. Chen, M. B. Hu, Q. C. Liang, K. Y. Yang, and M. K. Zhang, “A miniature multi-pulse series loading Hopkinson bar experimental device based on an electromagnetic launch,” *Rev. Sci. Instrum.*, vol. 90, no. 2, Feb. 2019, Art. no. 025110.
[17] S. Cai, D. L. Wu, J. F. Zhou, C. T. Zhang, Z. W. Liu, and S. Liu, “Improvement and application of miniature Hopkinson bar device based on series-parallel coil array electromagnetic launch,” *Measurement*, vol. 186, Dce. 2021, Art. no. 110203.
[18] H. L. Nie, T. Suo, B. B. Wu, Y. L. Li, and H. Zhao, “A versatile split Hopkinson pressure bar using electromagnetic loading,” *Int. J. Impact Eng.*, vol. 116, pp. 94-104, Jun. 2018.
[19] M. M. Khan and M. A. Iqbal, “Design, development, and calibration of split Hopkinson pressure bar system for dynamic material characterization of concrete,” *Int. J. Prot. Struct.*, vol. 15, no. 2, pp. 195-223, Jan. 2024.
[20] S. H. Zhao, *et al.*, “Design of a continuously repeated impact method with constant amplitude based on Hopkinson bar: Principle and impact fatigue life testing,” *Int. J. Impact Eng.*, vol. 193, Nov. 2024, Art. no. 105038.
[21] P. Quillery, B. Durand, M. Huang, K. Seck, and H. Zhao, “Dynamic biaxial compression tests using 4 symmetric input Hopkinson bars,” *Exp. Mech.*, vol. 64, no. 5, pp. 729-743, Oct. 2024.
[22] A. Kamble and P. Tandaiya, “Modeling and simulation of dynamic compression of bulk metallic glasses at room and elevated temperatures using split Hopkinson pressure bar setup,” *Int. J. Plast.*, vol. 174, Mar. 2024, Art. no. 103915.
[23] K. Sobczyk, R. Chmielewski, L. Kruszka, and R. Rekucki, “Strength characterization of soils’ properties at high strain rates using the Hopkinson technique-a review of experimental testing,” *Materials*, vol. 15, no. 1, Jan. 2022, Art. no. 274.
[24] S. R. Wang, X. G. Wu, J. H. Yang, J. Q. Zhao, and F. L. Kong, “Mechanical behavior of lightweight concrete structures subjected to 3D coupled static-dynamic loads,” *Acta Mech.*, vol. 231, no. 11, pp. 4497-4511, Nov. 2020.